



Broadband integrated polarization rotator using three-layer metallic grating structures

REN-HAO FAN,¹ DONG LIU,¹ RU-WEN PENG,^{1,3} WEN-BO SHI,¹ HAO JING,¹ XIAN-RONG HUANG,² AND MU WANG^{1,4}

¹National Laboratory of Solid State Microstructures, School of Physics, and Collaborative Innovation Center of Advanced Microstructures, Nanjing University, Nanjing 210093, China

²Advanced Photon Source, Argonne National Laboratory, Argonne, Illinois 60439, USA

³rwpeng@nju.edu.cn

⁴muwang@nju.edu.cn

Abstract: In this work, we demonstrate broadband integrated polarization rotator (IPR) with a series of three-layer rotating metallic grating structures. This transmissive optical IPR can conveniently rotate the polarization of linearly polarized light to any desired directions at different spatial locations with high conversion efficiency, which is nearly constant for different rotation angles. The linear polarization rotation originates from multi-wave interference in the three-layer grating structure. We anticipate that this type of IPR will find wide applications in analytical chemistry, biology, communication technology, imaging, etc.

© 2018 Optical Society of America under the terms of the [OSA Open Access Publishing Agreement](#)

OCIS codes: (050.2770) Gratings; (130.5440) Polarization-selective devices; (260.5430) Polarization.

References and links

1. F. Wikipedia, "Polarizer," <https://en.wikipedia.org/wiki/Polarizer>.
2. R. Yasuhara, I. Snetkov, A. Starobor, E. Mironov, and O. Palashov, "Faraday rotator based on TSAG crystal with <001> orientation," *Opt. Express* **24**(14), 15486–15493 (2016).
3. Z. Zhuang, Y. J. Kim, and J. S. Patel, "Achromatic linear polarization rotator using twisted nematic liquid crystals," *Appl. Phys. Lett.* **76**(26), 3995–3997 (2000).
4. H. Ren and S. T. Wu, "Liquid-crystal-based linear polarization rotator," *Appl. Phys. Lett.* **90**(12), 121123 (2007).
5. R. Desmarchelier, M. Lancry, M. Gecevicius, M. Beresna, P. G. Kazansky, and B. Poumellec, "Achromatic polarization rotator imprinted by ultrafast laser nanostructuring in glass," *Appl. Phys. Lett.* **107**(18), 181111 (2015).
6. M. R. Watts and H. A. Haus, "Integrated mode-evolution-based polarization rotators," *Opt. Lett.* **30**(2), 138–140 (2005).
7. D. Dai and J. E. Bowers, "Novel concept for ultracompact polarization splitter-rotator based on silicon nanowires," *Opt. Express* **19**(11), 10940–10949 (2011).
8. Q. Xu, L. Chen, M. G. Wood, P. Sun, and R. M. Reano, "Electrically tunable optical polarization rotation on a silicon chip using Berry's phase," *Nat. Commun.* **5**, 5337 (2014).
9. J. Y. Chin, M. Lu, and T. J. Cui, "Metamaterial polarizers by electric-field-coupled resonators," *Appl. Phys. Lett.* **93**(25), 251903 (2008).
10. Y. Ye and S. He, "90° polarization rotator using a bilayered chiral metamaterial with giant optical activity," *Appl. Phys. Lett.* **96**(20), 203501 (2010).
11. F. I. Baida, M. Boutria, R. Oussaid, and D. Van Labeke, "Enhanced-transmission metamaterials as anisotropic plates," *Phys. Rev. B* **84**(3), 035107 (2011).
12. S. Wu, Z. Zhang, Y. Zhang, K. Zhang, L. Zhou, X. Zhang, and Y. Zhu, "Enhanced rotation of the polarization of a light beam transmitted through a silver film with an array of perforated S-shaped holes," *Phys. Rev. Lett.* **110**(20), 207401 (2013).
13. Y. Yang, W. Wang, P. Moitra, I. I. Kravchenko, D. P. Briggs, and J. Valentine, "Dielectric meta-reflectarray for broadband linear polarization conversion and optical vortex generation," *Nano Lett.* **14**(3), 1394–1399 (2014).
14. S. C. Jiang, X. Xiong, Y. S. Hu, Y. H. Hu, G. B. Ma, R. W. Peng, C. Sun, and M. Wang, "Controlling the polarization state of light with a dispersion-free metastructure," *Phys. Rev. X* **4**(2), 021026 (2014).
15. Z. H. Jiang, L. Lin, D. Ma, S. Yun, D. H. Werner, Z. Liu, and T. S. Mayer, "Broadband and wide field-of-view plasmonic metasurface-enabled waveplates," *Sci. Rep.* **4**(1), 7511 (2014).
16. Y. Jia, Y. Liu, W. Zhang, and S. Gong, "Ultra-wideband and high-efficiency polarization rotator based on metasurface," *Appl. Phys. Lett.* **109**(5), 051901 (2016).
17. J. Y. Chin, T. Steinle, T. Wehler, D. Dregely, T. Weiss, V. I. Belotelov, B. Stritzker, and H. Giessen, "Nonreciprocal plasmonics enables giant enhancement of thin-film Faraday rotation," *Nat. Commun.* **4**, 1599 (2013).

- (2013).
18. D. Floess, J. Y. Chin, A. Kawatani, D. Dregely, H. U. Habermeier, T. Weiss, and H. Giessen, "Tunable and switchable polarization rotation with non-reciprocal plasmonic thin films at designated wavelengths," *Light Sci. Appl.* **4**(5), e284 (2015).
 19. Z. Marcet, H. B. Chan, D. W. Carr, J. E. Bower, R. A. Cirelli, F. Klemens, W. M. Mansfield, J. F. Miner, C. S. Pai, and I. I. Kravchenko, "A half wave retarder made of bilayer subwavelength metallic apertures," *Appl. Phys. Lett.* **98**(15), 151107 (2011).
 20. Y. Zhao, M. A. Belkin, and A. Alù, "Twisted optical metamaterials for planarized ultrathin broadband circular polarizers," *Nat. Commun.* **3**, 870 (2012).
 21. Y. Chiang and T. Yen, "A composite-metamaterial-based terahertz-wave polarization rotator with an ultrathin thickness, an excellent conversion ratio, and enhanced transmission," *Appl. Phys. Lett.* **102**(1), 011129 (2013).
 22. N. K. Grady, J. E. Heyes, D. R. Chowdhury, Y. Zeng, M. T. Reiten, A. K. Azad, A. J. Taylor, D. A. R. Dalvit, and H. T. Chen, "Terahertz metamaterials for linear polarization conversion and anomalous refraction," *Science* **340**(6138), 1304–1307 (2013).
 23. L. Cong, W. Cao, X. Zhang, Z. Tian, J. Gu, R. Singh, J. Han, and W. Zhang, "A perfect metamaterial polarization rotator," *Appl. Phys. Lett.* **103**(17), 171107 (2013).
 24. C. P. Huang, Q. J. Wang, X. G. Yin, Y. Zhang, J. Q. Li, and Y. Y. Zhu, "Break through the limitation of Malus' law with plasmonic polarizers," *Adv. Opt. Mater.* **2**(8), 723–728 (2014).
 25. X. Ma, W. Pan, C. Huang, M. Pu, Y. Wang, B. Zhao, J. Cui, C. Wang, and X. Luo, "An active metamaterial for polarization manipulating," *Adv. Opt. Mater.* **2**(10), 945–949 (2014).
 26. R. H. Fan, Y. Zhou, X. P. Ren, R. W. Peng, S. C. Jiang, D. H. Xu, X. Xiong, X. R. Huang, and M. Wang, "Freely tunable broadband polarization rotator for terahertz waves," *Adv. Mater.* **27**(7), 1201–1206 (2015).
 27. Z. Li, S. Chen, W. Liu, H. Cheng, Z. Liu, J. Li, P. Yu, B. Xie, and J. Tian, "High performance broadband asymmetric polarization conversion due to polarization-dependent reflection," *Plasmonics* **10**(6), 1703–1711 (2015).
 28. C. P. Huang, "Efficient and broadband polarization conversion with the coupled metasurfaces," *Opt. Express* **23**(25), 32015–32024 (2015).
 29. J. Wang, Z. Shen, and W. Wu, "Cavity-based high-efficiency and wideband 90° polarization rotator," *Appl. Phys. Lett.* **109**(15), 153504 (2016).
 30. A. Taflove and S. C. Hagness, *Computational Electrodynamics: The Finite-Difference Time-Domain Method* (Artech House, 2005).
 31. Y. Zhang, J. Z. Zhu, C. P. Huang, and S. J. Ma, "Wide-band and high-efficiency 90° polarization rotator based on tri-layered perforated metal films," *J. Lightwave Technol.* **35**(21), 4817–4823 (2017).

1. Introduction

Light can be used as a carrier of information based on its basic physical attributes. For example, people can distinguish different objects based on their color and brightness patterns, which originate from their response to different wavelengths (or frequencies) and intensities of light. The spatial structure can also be perceived from the propagation direction of light. Holographic display is an important type of three-dimensional (3D) display that relies on the spatial phase information of light. Polarization is also a basic physical attribute of light; however, it has not yet been widely used to transfer spatial information mainly due to the lack of spatially integrated broadband polarization modulators. Specifically, if a spatially-integrated broadband polarization rotator could be realized, we may transfer spatial information by tuning the polarization directions at different spatial locations. This type of integrated polarization rotator (IPR) may have wide applications in analytical chemistry, biology, communication technology, imaging, etc. For example, biomolecules on earth are generally composed of sinistral amino acids and dextral carbohydrates, which lead to complex optical rotation characteristics. In a biomolecule application, integrated polarization rotators can be fabricated as biomolecule detection chips that can identify biomolecules with different polarization responses.

Essentially a broadband integrated polarization rotator (IPR) should possess two characteristics. The first is the ability to combine many units into a single small device, each of which can rotate the polarization of linear polarized light in any desired direction. The second is that these units should have high and nearly constant conversion efficiency for different rotation angles. Traditionally, polarization rotators are constructed using two polarizers [1], magneto-optical materials [2], liquid crystals [3, 4], multiple-stacked birefringent layers [5], waveguides [6–8], and so on. Nonetheless, these devices are usually bulky. Recently, the use of microstructures enables the rotation of the polarization of light

without employing bulky devices, and linear polarization rotation has now been achieved using metamaterials [9, 10], single perforated metal films [11, 12], metasurfaces [13–16], thin-film Faraday rotators [17, 18], and composite structures consisting of multilayered microstructures [19–29]. Among them, the composite structure is a basic unit that can potentially be used in a spatially integrated broadband polarization rotator; however, no such microstructure-based device has been fabricated to date.

In this work, we demonstrate a broadband integrated polarization rotator (IPR) using three-layer rotating metallic grating structures. First of all, we show a broadband 90-degree polarization rotator using this three-layer rotating metallic grating structure, and discuss the physical mechanisms under this polarization rotation. Then, we extend the 90-degree polarization rotation to other situations, this is a transmissive optical polarization rotator that can rotate the polarization of linearly polarized light to any desired direction with high and nearly constant conversion efficiency. Finally, we demonstrate a broadband IPR based on these polarization rotators.

2. A broadband 90-degree polarization rotator using three-layer metallic grating structure

2.1 Structural design, sample fabrication and optical measurements

A broadband 90-degree polarization rotator can be made using three-layer metallic grating structure as shown in Fig. 1. The first, second, and third gratings, which are respectively denoted S1, S2, and S3, have various periods d_1 , d_2 , and d_3 , but the same slit widths w . The thicknesses of the gratings and the dielectric space between the neighboring grating layers are h and s , respectively, and the same dielectric material is used in all grating slits. The rotation angle between S1 and S2 is $\varphi_{12} = 45^\circ$, and that between S2 and S3 is $\varphi_{23} = 45^\circ$. This 90-degree polarization rotator can rotate the linearly polarized light to its crossed direction.

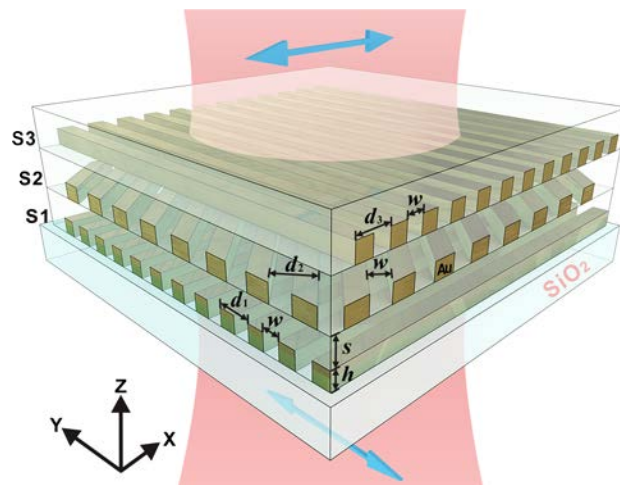


Fig. 1. Schematic of the broadband 90-degree polarization rotator.

Numerical calculations based on the finite-difference time-domain (FDTD) method [30] were also carried out with the commercially available Lumerical FDTD Solution 8.0.1 software package. The permittivity of gold was obtained from the Johnson and Christy model, and the refractive index of silicon dioxide, which was used for the substrate and the dielectric material, was set to 1.455 in the calculations. In our testing, the incident light exhibited a transverse-magnetic (TM) polarization with an electric field \mathbf{E}_0 (along Y axis) perpendicular to the strips of the first grating. We defined the angle $\Phi = \varphi_{12} + \varphi_{23}$ as the designed total linear polarization rotation angle, which means that the linear polarization state of the incident beam can be rotated by an angle Φ after transmission. $\Phi = 90^\circ$ for this 90-degree polarization

rotator, that is to say the polarization can be rotated from Y axis to X axis. The transmitted electric field can be expressed as $\mathbf{E} = \mathbf{E}_{//}(\Phi) + \mathbf{E}_{\perp}(\Phi)$, where $\mathbf{E}_{//}(\Phi)$ and $\mathbf{E}_{\perp}(\Phi)$ are the components that were polarized parallel and perpendicular to the designed polarization direction, respectively. For example, $\mathbf{E}_{//}(90^\circ)$ means the electric field parallel to the designed direction (X axis for this 90-degree polarization rotator), and $\mathbf{E}_{\perp}(90^\circ)$ corresponds to the polarization along Y axis for this case. In order to verify the polarization rotation induced by the device, we also defined two parameters $T_{//}(\Phi) = |\mathbf{E}_{//}(\Phi)|^2 / |\mathbf{E}_0|^2$ and $T_{\perp}(\Phi) = |\mathbf{E}_{\perp}(\Phi)|^2 / |\mathbf{E}_0|^2$ to represent the transmissivity components along the two orthogonal directions.

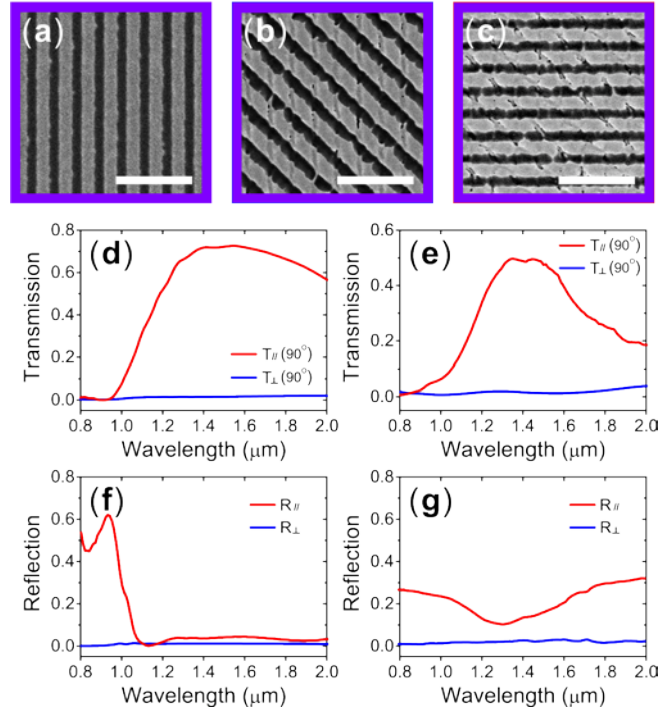


Fig. 2. SEM images of the broadband 90-degree polarization rotator sample: (a) SEM image of the first grating layer S1; (b) SEM image of the second grating layer S2; (c) SEM image of the third grating layer S3. In all images, the scale bar is $1 \mu\text{m}$. (d) Calculated and (e) measured transmission components $T_{//}(90^\circ)$ and $T_{\perp}(90^\circ)$ of this polarization rotator. (f) Calculated and (g) measured reflection components $R_{//}$ and R_{\perp} of this polarization rotator. The electric field of the incident light along Y axis, $d_1 = d_3 = 300 \text{ nm}$, $d_2 = 350 \text{ nm}$, $w = 125 \text{ nm}$, $h = 30 \text{ nm}$, and $s = 60 \text{ nm}$.

During sample fabrication, we first applied a 30-nm thick gold film ($h = 30 \text{ nm}$) to K9 optical glass by magnetron sputtering. Then, a focused-ion-beam facility (FIB, Helios Nanolab 600i) was used to mill the grating structure S1, with $d_1 = 300 \text{ nm}$, and $w = 125 \text{ nm}$. Then, a 120-nm thick silicon dioxide film was applied to the surface of S1, and inductively coupled reactive ion etching (ICP-RIE, ULVAC CE300I) was used to reduce the thickness of the silicon dioxide film to about 60 nm ($s = 60 \text{ nm}$), thereby smoothing the surface of the silicon dioxide film. A 30-nm thick gold film was applied on top of the 60-nm silicon dioxide film, then, we employed the FIB to mill the S2 grating structure a second time, with $d_2 = 350 \text{ nm}$, and $w = 125 \text{ nm}$. A 60-nm thick silicon dioxide film was applied on top of S2, and the S3 grating structure was fabricated using the same process, with $d_3 = 300 \text{ nm}$, and $w = 125 \text{ nm}$. Finally, a 60-nm thick silicon dioxide film was applied on top of the S3 layer to fill in the grating slits. The SEM images of the first, second, and third grating layers (S1, S2, and S3)

are shown in Figs. 2(a)-2(c), respectively. The parameters of this sample come from the optimized results of the numerical calculation, the calculated results shown in Fig. 2(d) indicate that $T_{\perp}(90^{\circ})$ was less than 2.0% between 1.25 μm and 1.95 μm ; while $T_{\parallel}(90^{\circ})$ was much higher than $T_{\perp}(90^{\circ})$, the calculated $T_{\parallel}(90^{\circ})$ was larger than 60% between 1.25 μm and 1.95 μm . The calculated polarization ratio is higher than 30:1 between 1.25 μm and 1.95 μm .

A microspectrophotometer (Craic, QDI2010) was used to measure the optical spectra of the samples. We use the polarizer to generate the polarized light with electric field along Y axis, and use the analyzer before the detector to choose transmission component to be detected. When the polarizer parallel to analyzer, we can detect very low transmission intensity, the detected $T_{\perp}(90^{\circ})$ was less than 3.4% between 1.25 μm and 1.95 μm . When the polarizer perpendicular to analyzer, we can detect high transmission intensity $T_{\parallel}(90^{\circ})$ between 1.25 μm and 1.95 μm . The measured transmission components in Fig. 2(e) correspond to the calculations in Fig. 2(d), although with slightly lower values of $T_{\parallel}(90^{\circ})$, which were primarily due to defects in the sample after multiple processing cycles of magnetron sputtering and FIB.

In order to explore which factors affect the efficiency of this 90-degree polarization rotator, we also defined two parameters $R_{\parallel} = |\mathbf{E}_{\parallel}|^2 / |\mathbf{E}_0|^2$ and $R_{\perp} = |\mathbf{E}_{\perp}|^2 / |\mathbf{E}_0|^2$ to represent the reflection components along the two orthogonal directions, where \mathbf{E}_{\parallel} and \mathbf{E}_{\perp} are the components that were polarized parallel (along Y axis) and perpendicular (along X axis) to the incident light, respectively. The calculated and measured reflection components R_{\perp} are very low as shown in Figs. 2(f) and 2(g), which means no polarization rotation happened for the reflection light. Meanwhile, the calculated R_{\parallel} is lower than 5% between 1.25 μm and 1.95 μm , which means the loss of the metal is the main cause that reduce the efficiency of this rotator. Moreover, the measured R_{\parallel} in Fig. 2(g) is larger than the calculated results, this difference comes from the defects of the sample, and further reducing the efficiency of this 90-degree polarization rotator.

2.2 Theoretical analysis

To better understand the physics underlying this broadband 90-degree polarization rotation, we calculated the near field distribution of electric field intensity $|\mathbf{E}_x|^2$ and $|\mathbf{E}_y|^2$ at $\lambda = 1310$ nm, as shown in Fig. 3. The incident light with electric field component along Y axis passes through S1. At S2, the wave with electric field component parallel to the strip of S2 (45° to X axis) is reflected back, and it has both $|\mathbf{E}_x|^2$ and $|\mathbf{E}_y|^2$, which can be seen in Figs. 3(c) and 3(d). The reflected wave has the grating patterns corresponding to S2. Then the wave $|\mathbf{E}_x|^2$ reflected back by S2 is reflected back again by S1, and the wave $|\mathbf{E}_y|^2$ reflected back by S2 can pass through S1 to form reflection wave r_1 . At S2, the wave with electric field component perpendicular to the strip of S2 (-45° to X axis) can pass through S2, and it has both $|\mathbf{E}_x|^2$ and $|\mathbf{E}_y|^2$ which can be seen in Figs. 3(e) and 3(f). The transmitted wave has the grating patterns corresponding to S2 as well. At S3, the wave $|\mathbf{E}_x|^2$ can pass through to form transmission wave t_1 , and the wave $|\mathbf{E}_y|^2$ is reflected back to S2 again by S3.

Those transmission and reflection processes repeat over and over. The waves travel back and forth between S1 and S2, and finally passing through S1 to form a series of reflection waves r_i ($i = 1, 2, 3, \dots, n$). Other parts of waves travelling between S2 and S3 eventually pass through S3 to form a series of transmission waves t_i ($i = 1, 2, 3, \dots, n$). The destructive interference of multiple reflection waves $r_1, r_2, r_3, r_4, r_5, \dots, r_n$ can lead to the low reflection of the rotator, while the constructive interference of multiple transmission waves $t_1, t_2, t_3, t_4, t_5, \dots, t_n$ can lead to a high efficiency polarization conversion. Within this tri-grating structure, the waves with electric fields $|\mathbf{E}_x|^2$ and $|\mathbf{E}_y|^2$ are inter-changeable, this inter-changeable comes from the near-field coupling as shown by Zhang *et al.* under the condition $s \ll \lambda$ [31]. The

three gratings S1, S2 and S3 can no longer be considered as separated gratings, instead they interact with each other to become a whole system, and result in changing the polarization of the incident light though near field coupling. Finally, the incident light with electric field along Y axis shown in Figs. 3(a) and 3(b) is changed to the transmission light with electric field along X axis shown in Figs. 3(g) and 3(h), perfect polarization conversion is realized at the optimal geometry. Therefore, based on our theoretical analysis, we conclude that this polarization rotation originates from multi-wave interference progress.

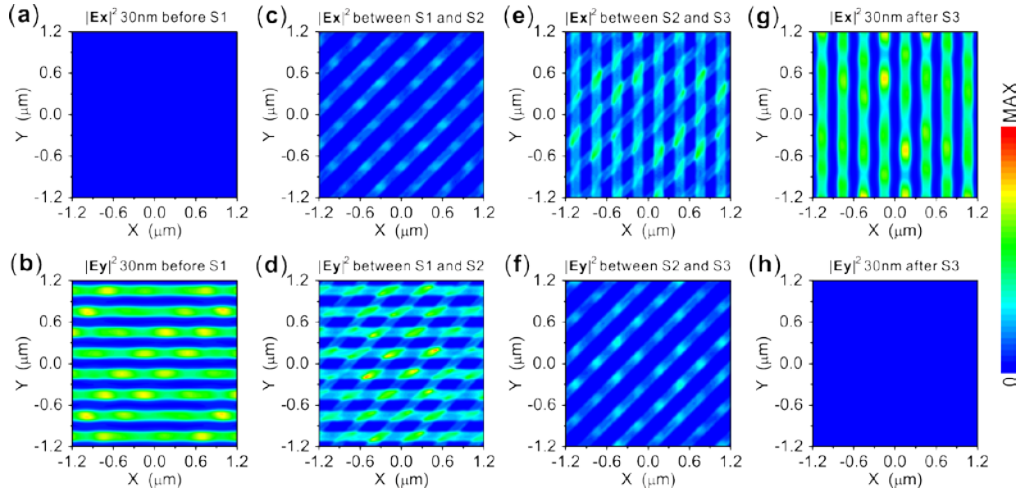


Fig. 3. The cross-sectional distribution of the electric fields at $\lambda = 1310$ nm: (a) $|\mathbf{E}_x|^2$ and (b) $|\mathbf{E}_y|^2$ 30 nm before S1; (c) $|\mathbf{E}_x|^2$ and (d) $|\mathbf{E}_y|^2$ between S1 and S2; (e) $|\mathbf{E}_x|^2$ and (f) $|\mathbf{E}_y|^2$ between S2 and S3; (g) $|\mathbf{E}_x|^2$ and (h) $|\mathbf{E}_y|^2$ 30 nm after S3. The electric field of the incident light along Y axis, $d_1 = d_3 = 300$ nm, $d_2 = 350$ nm, $w = 125$ nm, $h = 30$ nm, and $s = 60$ nm.

To discuss the working bandwidth of this 90-degree polarization rotator, we calculate the averaged near field electric intensity $|\mathbf{E}_x|^2$ and $|\mathbf{E}_y|^2$ among the cross sections from $0.80 \mu\text{m}$ to $2.00 \mu\text{m}$ as shown in Fig. 4. Before the rotator, the $|\mathbf{E}_x|^2$ is nearly 0 as shown in Fig. 4(a) and the $|\mathbf{E}_y|^2$ is high between $1.25 \mu\text{m}$ and $1.95 \mu\text{m}$ as shown in Fig. 4(b), which shows the electric field of the incident light along Y axis. There exist both averaged electric field intensity $|\mathbf{E}_x|^2$ and $|\mathbf{E}_y|^2$ between the rotator as shown in Figs. 4(c)–4(f). However, after the rotator, the $|\mathbf{E}_x|^2$ is high between $1.25 \mu\text{m}$ and $1.95 \mu\text{m}$ as shown in Fig. 4(g) and the $|\mathbf{E}_y|^2$ is nearly 0 as shown in Fig. 4(h), the electric field of the transmission light changed to X axis, which shows a broadband 90-degree polarization rotation. Combined with the calculated transmission components $T_{//}(90^\circ)$ and $T_{\perp}(90^\circ)$ shown in Fig. 2(d), we conclude the working bandwidth of this 90-degree polarization rotator is from $1.25 \mu\text{m}$ to $1.95 \mu\text{m}$, a high polarization rotation efficiency larger than 60% is happened within this region.

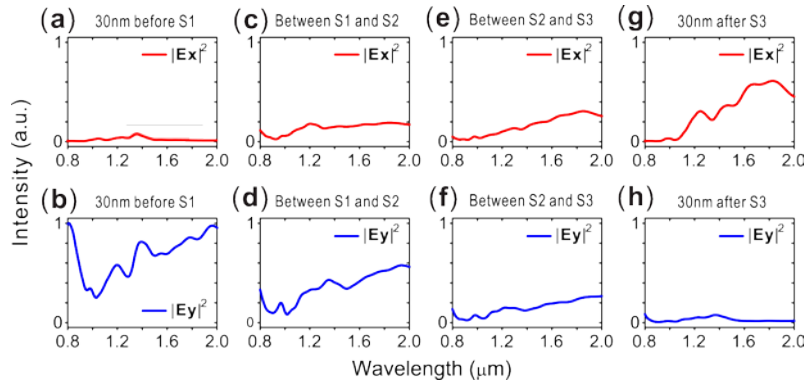


Fig. 4. The averaged electric fields $|E_x|^2$ and $|E_y|^2$ among the cross section: (a) and (b) 30nm before S1; (c) and (d) between S1 and S2; (e) and (f) between S2 and S3; (g) and (h) 30nm after S3. The electric field of the incident light along Y axis, $d_1 = d_3 = 300$ nm, $d_2 = 350$ nm, $w = 125$ nm, $h = 30$ nm, and $s = 60$ nm.

3. Broadband integrated polarization rotator

Up to now, we have demonstrated a broadband 90-degree polarization rotator using three-layer metallic grating structure. Actually, this is a transmissive optical polarization rotator that can rotate the polarization of linearly polarized light to any desired direction (not only 90°) with high conversion efficiency. By rotating the three composite grating layers, the polarization rotation angle Φ of the rotator can be tuned to any desired angle. So we can design a broadband integrated polarization rotator (IPR) consists of a series of rotator units, as shown in Fig. 5, each of which can rotate the linearly polarized light to one desired direction. The polarization direction of the transmission is mainly controlled by the rotation angle between the first and third gratings, the rotation angle $\Phi = \varphi_{12} + \varphi_{23}$, here, we set $\varphi_{12} = \varphi_{23} = \Phi/2$ in this work. We fix the first grating S1 and rotating the gratings S2 and S3, the incident light is TM-polarized with respect to the first grating S1.

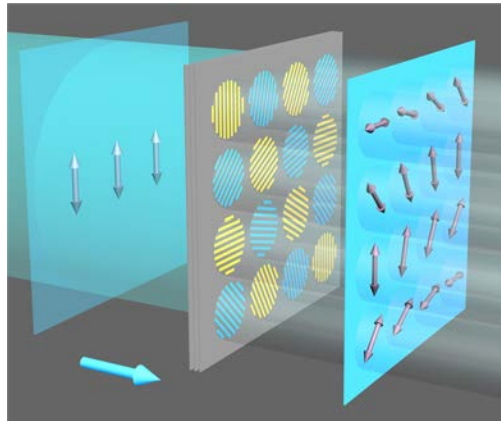


Fig. 5. Schematic of the broadband integrated polarization rotator.

The calculated $T_{//}(\Phi)$ and $T_{\perp}(\Phi)$ of the broadband polarization rotator when Φ varies from 0° to 90° are shown in Fig. 6, the incident light is TM-polarized with respect to the first grating S1. For all rotation angles Φ , high $T_{//}(\Phi)$ was happened around 1.20–2.00 μm , while the $T_{\perp}(\Phi)$ was less than 2.0% (actually, it was less than 1.0% for most situations) in this region. When rotating the gratings S2 and S3, the thickness of the gratings (h) and dielectric space (s) are not changed. Therefore, the phase difference of each transmission waves t_1 , t_2 , t_3 ,

t_4, t_5, \dots, t_n is fixed for the same wavelength, leading to the similar transmission intensity and working band of each rotator, so the intensity of $T_{//}(\Phi)$ does not change vary much when Φ varies from 0° to 90° , which means that the efficiency of the rotators will remain essentially the same for all situations.

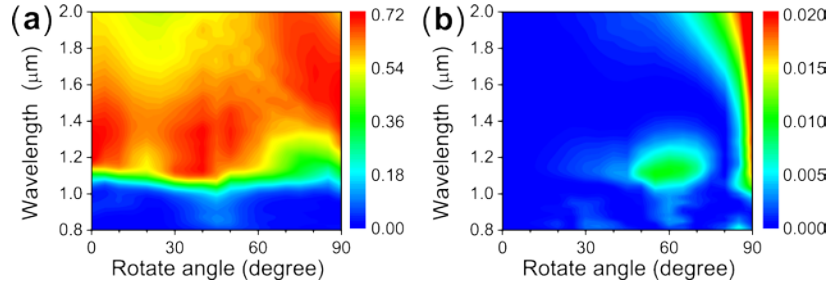


Fig. 6. Calculated transmission components: (a) $T_{//}(\Phi)$ and (b) $T_{\perp}(\Phi)$ of the polarization rotator with varying angles Φ from 0° to 90° . The color bars show their intensity levels. The incident light is TM-polarized with respect to the first grating S1, $d_1 = d_3 = 300$ nm, $d_2 = 350$ nm, $w = 125$ nm, $h = 30$ nm, and $s = 60$ nm.

As mentioned above, the polarization of the rotator unit can be tuned to any desired direction by rotating the three composite grating layers, all of which have nearly the same rotation efficiency and working bandwidth. Consequently, a broadband IPR can be fabricated with series rotators on the same substrate but with different rotation angles. As an example, the photograph of a fabricated IPR is shown in Fig. 7(a). This integrated rotator combines five rotators with angles of $\Phi = 0^\circ, 30^\circ, 45^\circ, 60^\circ,$ and 90° , respectively. It can be seen that the measured transmission components $T_{//}(\Phi)$ and $T_{\perp}(\Phi)$ for $\Phi = 0^\circ, 30^\circ, 45^\circ, 60^\circ,$ and 90° have nearly the same intensity from 1.20 to 2.00 μm , as shown in Fig. 7, which means the conversion efficiency is nearly constant for different rotation angles. And it is a subwavelength device with 270nm thickness, which is less than one quarter of the central wavelength ($\lambda = 1.6\mu\text{m}$) in the working band. People can get the spatially different light using this IPR; the spatially difference among the transmitted light is only the polarization direction.

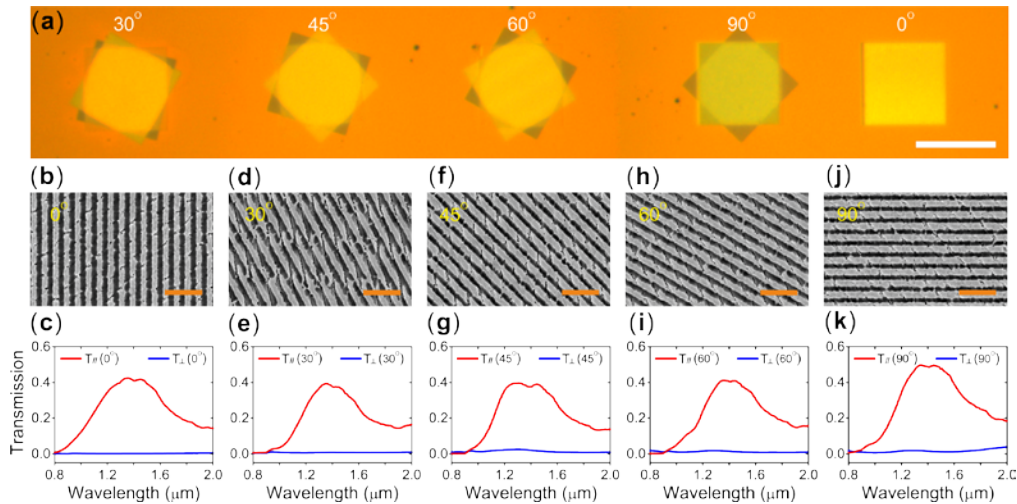


Fig. 7. (a) Photograph of a broadband IPR that combines five rotators with $\Phi = 30^\circ, 45^\circ, 60^\circ, 90^\circ,$ and 0° , the white scale bar is 50 μm . SEM images and the measured $T_{//}(\Phi)$ and $T_{\perp}(\Phi)$ of the rotators: (b) and (c) $\Phi = 0^\circ$; (d) and (e) $\Phi = 30^\circ$; (f) and (g) $\Phi = 45^\circ$; (h) and (i) $\Phi = 60^\circ$; (j) and (k) $\Phi = 90^\circ$. The orange scale bar is 1 μm , the incident wave is TM-polarized with respect to the first grating S1, $d_1 = d_3 = 300$ nm, $d_2 = 350$ nm, $w = 125$ nm, $h = 30$ nm, and $s = 60$ nm.

4. Conclusion

In summary, we have experimentally demonstrated a broadband IPR using three-layer rotating metallic grating structure. Firstly, we demonstrated a broadband 90-degree polarization rotator using three-layer metallic grating structure, the working bandwidth of this 90-degree polarization rotator is from 1.25 μm to 1.95 μm with a high polarization rotation efficiency which is larger than 60% within this region. Secondly, we find this three-layer metallic grating structure can conveniently rotate the polarization of linearly polarized light to any desired direction with high and nearly constant conversion efficiency. Finally, we have demonstrated a broadband IPR using these three-layer rotating metallic grating structures, it is a subwavelength device with a thickness of 270 nm, which is less than one quarter of the central wavelength in the working band around 1.20–2.00 μm . This polarization rotation was found to originate from multi-wave interference in the three-layer grating structure. The same principle can be used to design broadband IPR at other frequency region. We anticipate that this type of broadband IPR may find applications in analytical chemistry, biology, communication technology, imaging, etc.

Funding

National Key R&D Program of China (2017YFA0303702); National Natural Science Foundation of China (11634005, 11604143, 61475070, 11474157, 11674155, 11621091); Ministry of Science and Technology of China (2014CB921103); “333 project” from Jiangsu province (BRA2016350); China Postdoctoral Science Foundation (Grant No. 2015T80533); U.S. Department of Energy, Office of Science, Office of Basic Energy Sciences (DE-AC02-06CH11357).